Three-dimensional Rigorous Simulation of EUV Defective Masks Using Modal Method by Fourier Expansion

Rafik Smaali, Besacier Maxime, Schiavone Patrick

To cite this version:

Rafik Smaali, Besacier Maxime, Schiavone Patrick. Three-dimensional Rigorous Simulation of EUV Defective Masks Using Modal Method by Fourier Expansion. Proceedings of SPIE, the International Society for Optical Engineering, 2006, Emerging Lithographic Technologies X, 6151, ⟨10.1117/12.655495⟩. ⟨hal-04286869⟩

HAL Id: hal-04286869
https://hal.science/hal-04286869v1

Submitted on 15 Nov 2023

HAL is a multi-disciplinary open access archive for the deposit and dissemination of scientific research documents, whether they are published or not. The documents may come from teaching and research institutions in France or abroad, or from public or private research centers.

L'archive ouverte pluridisciplinaire **HAL**, est destinée au dépôt et à la diffusion de documents scientifiques de niveau recherche, publiés ou non, émanant des établissements d'enseignement et de recherche français ou étrangers, des laboratoires publics ou privés.

Autorisation HAL

HAL Authorization

Three-dimensional Rigorous Simulation of EUV Defective Masks Using Modal Method by Fourier Expansion

Rafik Smaali, Maxime Besacier, Patrick Schiavone

Laboratoire des Technologies de la Microélectronique CNRS, c/o CEA Grenoble, 17 Avenue des Martyrs, 38054 Grenoble Cedex 09, France

ABSTRACT

In Extreme Ultraviolet Lithography, the electromagnetic modelling of the mask allows determining the influence of the mask structure on the electromagnetic field. That makes it possible to take into account the presence of a defect modifying the multi-layer stack[1,2]. The method used troughout this paper is the MMFE (Modal Method by Fourier Expansion) also known as the RCWA (Rigorous Coupled Wave Analysis). Modal methods allow computing the electromagnetic field just above the EUV mask or the near field. Modal methods are well adapted for EUV mask simulation due to materials and structure size. The previous works performed on 2D simulation with MMFE[3] have shown the influence of a defect inside a EUV mask structure. In this article, the method is extended to address 3D structures. The printability of a spherical shaped defect is analyzed depending on the deposition process used. The influence of a 3D defect position regarding the position of a line absorber is also shown.

Keywords: EUV Lithography, 3D electromagnetic simulation, defective mask, modal method, absorber pattern, aerial image.

1. INTRODUCTION

EUV mask manufacturing remains a challenge in the perspective of the EUV lithography development for the next integrated circuit generation. One of the main reasons of this difficulty is the presence of particles inside the Molybdenum and Silicium reflective multilayer stack of the mask blank. These particles appear during the deposition process and it is difficult to monitor their density. These particles are considered like defects because, in spite of their small size, they can disturb the very precise deposition of each layer and then disturb the periodicity of the Bragg mirror. Some experiments using programmed defects have been performed. These experiments underline the importance of the deposition process. Some techniques combine etching and smoothing to reduce defect influence[4] and other using nonsmoothing process are focused on the growth of defects within the multilayer [5,6,7]. The results show that the understanding of printability is not a simple task and depends on the defects characteristics such as the shape or the size but also significantly on the deposition process. Considering these difficulties, simulation is a convenient way to predict if the defect will be printed on the resist or not. To pretend on confident simulation results, models that describe the input geometry inserted in the electromagnetic simulation tools have to be as close to the real structure as possible. The 2D simulations are not adequate because of the obvious 3D shape of a defect. The deposition process, it means how the defect is propagated through the layers, must also be modelled with fidelity.

The possible printability of a defect is observed on the cross section of the resulting aerial image for a chosen threshold. The modal method gives the near field characteristics. The aerial image is computed using a software tool provided by the simulation group of the Fraunhofer Institut in Erlangen.

In the first part of the paper, the main modifications needed for the extension to 3D extension of the electromagnetic simulation code is described as well as the computation performance. The second section deals with the presence of a 3D defect inside the Si/Mo multilayer stack. In this paper, the shape of the defect is considered spherical, but other shapes can be handled by the code as well. The parameter used to define this kind of defect is the diameter. In this second part, a presentation of the model to consider the deposition process is also included. The study of the printability is done regarding the obtained aerial image. The third part considers the printability of a defect in presence of, first an absorber line and secondly an absorber post deposited on top of the defective multilayer structure. The influence of the relative position of the defect with respect to the absorber position is studied.

2. MODAL METHOD BY FOURIER EXPANSION IN 3D

2.1. 3D extension

Regarding the computation of 2D structures, accounting for a new dimension in the modelling structure does not change the global approach of the problem but several news parameters must be considered in the equations. It leads to a more complex problem and the code development must be done carefully not to increase the computation time exceedingly. This aspect of the code is not developed in this article but is to be kept it in mind.

The 3D approach is presented in Figure 1 with the slice cut which is typical to MMFE computation. A monochromatic, linearly polarized, incident plane wave, with a wavelength λ, illuminates the grating with a propagation direction specified by polar angle θ and azymutal angle ϕ (Figure 2).

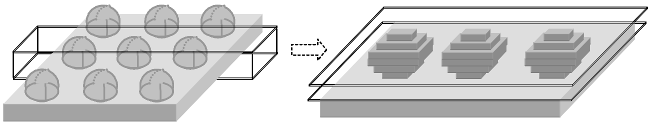

Figure 1 : zoom of a 3D structure cut in slices

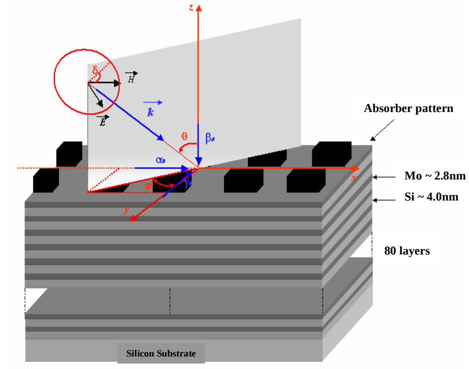

Figure 2 : 3D structure of EUV mask with incident light description

The components of the incident wave vector are:

$k_x = k_0.\sin\theta.\cos\phi$

$k_y = k_0.\ \sin\theta.\sin\phi$

$k_z = -k_0.\ \cos\theta$

The angle δ between the magnetic field vector and the plane of incidence defines the direction of polarization.

The first step of the MMFE, also known as the rigorous coupled wave analysis[8,9,10] (RCWA), is to find a solution of Maxwell equations in each region (homogeneous and grating region).

In the grating region, we use the same approach than in the article of Granet[11], and the following second-order eigenvalue equation is written:

$$\partial_z^2 \begin{bmatrix} E_x \\ E_y \end{bmatrix} = \Im_{EH}\Im_{HE}(x,y) \begin{bmatrix} E_x \\ E_y \end{bmatrix} \qquad (\text{Eq. } 1)$$

with

$$\Im_{EH} = \begin{bmatrix} \frac{i}{k}\partial_x(\varepsilon)^{-1}\partial_y & -\frac{i}{k}\partial_x(\varepsilon)^{-1}\partial_x - ik \\ \frac{i}{k}\partial_y(\varepsilon)^{-1}\partial_y + ik & -\frac{i}{k}\partial_y(\varepsilon)^{-1}\partial_x \end{bmatrix} \text{ and } \Im_{HE} = \begin{bmatrix} -\frac{i}{k}\partial_x\partial_y & ik\left\lceil \lfloor \varepsilon \rfloor \right\rceil + \frac{i}{k}\partial_x^2 \\ -ik\left\lfloor \lceil \varepsilon \rceil \right\rfloor - \frac{i}{k}\partial_y^2 & \frac{i}{k}\partial_y\partial_x \end{bmatrix} \qquad (\text{Eq. } 2)$$

It should be emphasized that the matrix associated with the $\Im_{EH}$ and $\Im_{HE}$ operator must follow the factorization rules given by Li[12].

Any component F of the electric or magnetic field can be expressed as a superposition of eigenmode fields

$$F(x,y,z) = \sum_p (A_p^+ \exp -ik\gamma_p z + A_p^- \exp ik\gamma_p z) \sum_{m,n} F_{mn} e_{mn}(x,y) \quad (\text{Eq. } 3)$$

with

$$e_{mn}(x,y) = exp(-ik\alpha_m x)\exp(-ik\beta_n y) \quad (\text{Eq. } 4)$$

$$k\alpha_m = k_x + m\frac{2\pi}{d_x}, \quad k\beta_n = k_y + n\frac{2\pi}{d_y} \quad \text{(Eq. 5)}$$

A_p^+ and A_p^- are the unknown complex amplitudes of the upward and the downward propagating or decaying fields. If the truncation is described by $-M \leq m \leq M$ and $-N \leq n \leq N$, where M and N are integers, the rank of the matrix from which eigenvalues and vectors are computed is 2.(2.M+1).(2.N+1). In our numerical computations, M=N is chosen.

In the homogeneous regions, the second-order eigenvalue equation (Eq. 1) is written with a new operator

$$\Im_E = \Im_{EH}\Im_{HE} = \begin{bmatrix} -\partial_x^2 - \partial_y^2 - k^2\varepsilon & 0 \\ 0 & -\partial_x^2 - \partial_y^2 - k^2\varepsilon \end{bmatrix} \quad \text{(Eq. 6)}$$

Since the $\Im_E$ operator is diagonal, E_x and E_y are two independent components. These two components do not follow the same eigen equation. Finally, in a homogeneous medium, the electric and magnetic field components can be written as

$$E_x(x,y,z) = \sum_p (A_p^+ \exp - ik\gamma_p z + A_p^- \exp ik\gamma_p z)\sum_{m,n} E_{xmn} e_{mn}(x,y) \quad \text{(Eq. 7)}$$

$$H_x(x,y,z) = \sum_p (B_p^+ \exp - ik\gamma_p z + B_p^- \exp ik\gamma_p z)\sum_{m,n} H_{xmn} e_{mn}(x,y) \quad \text{(Eq. 8)}$$

Numerical experiments show that every eigenvalue γ_p^2 is linked to a pair (α_m, β_n) with to the following relationship:

$$\gamma_p^2 + \alpha_m^2 + \beta_n^2 = \varepsilon \quad \text{(Eq. 9)}$$

The last step of the MMFE, is to compute the amplitude of the field with the S matrix propagation algorithm.

2.2. Performance of the MMFE in 3D

The 3D extension of the modal method is a significant improvement to simulate the real behaviour of the modelled structure. Nevertheless this progress is very costly in computation time. However, in the EUV lithography domain, where the wavelength is close to the feature size, it allows addressing problems that the classical FDTD method is not able to solve. The performance of the code can be represented in term of convergence and computation time according the number of truncation order.

2.2.1. Convergence

The retained structure for the test of convergence of the MMFE in 3D is a grating of absorber dots deposited on a multilayer. The incidence angles are $\theta = 7°$, $\phi = 0°$, $\delta = 180°$.

The diffraction efficiency of the zero order is the parameter used to establish the limit of convergence. Figure 3 shows for three different values of pitches in the x and y direction the minimum number of truncation order to consider computing correctly the electromagnetic field.

It appears that for small pitches the convergence is achieved faster. For 100nm pitches, the convergence is achieved with a truncation order close to 5. For 200nm pitches the truncation order is close to 9.

2.2.2. Computation time

Compared to the 2D simulations, the computation time for 3D simulations has drastically increased. Figure 4 shows the time needed to compute an electromagnetic near field using a 3.2GHz PC under windows OS. The current version of the code is written in Matlab. It reaches large values if the number of slices is important. This is especially true when structures of defective multilayers are modelled. Indeed, the following part will show that a defect inserted inside the multilayer disturbs the deposition of layers. It leads to a smooth perturbation of the interface of the layers that requests a larger number of slices to be described. The structure of reference is the same than the one used for the convergence tests.

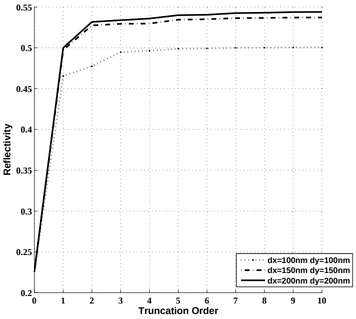

Figure 3 : Diffraction efficiency vs truncation order M for different values of d_x and d_y

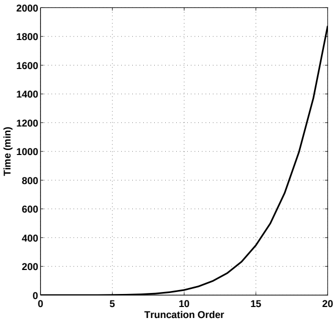

Figure 4 : Computation time vs truncation order

The near field above a EUV mask with a grating of dots can be computes within about 30 minutes for a truncation order M=10. This value allows for reaching convergence. The intensity of this reflected near field is represented in the Figure 5.

The features of this simulation are the following: near field intensity of a grating of dots, period=256nm, dot size=128nm, θ=5°, ϕ=0°, δ=180°, λ=13.5nm, absorber: 50nm chromium, 40 pairs of Mo 2.74nm/Si 4.11nm.

The computation time becomes larger for more complex structure. For instance, to address a defective multilayer structure, the computation time reaches about 8 hours.

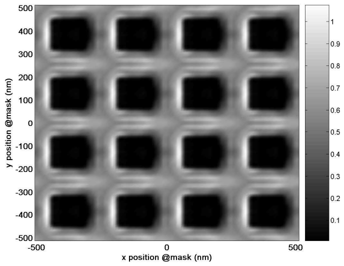

Figure 5 : Intensity of the near field above an EUV mask with a grating of dots

3. SIMULATION OF 3D DEFECTS IN SI/MO MULTILAYERS

3.1. Input geometry for EUV defective masks

The propagation of the defect inside the different layers must be described as close as possible to the real geometry. Article[13] have shown how it is difficult to define a global method able to model this propagation accurately. Indeed, depending on the size and the shape of the defect, but also on the deposition process used, the influence of the defect through the multilayer deposition can lead to very different behaviours.

Nevertheless, by using the parametric equations of the parallel curves in 3D, as defined below, we assume that the behaviour of a defect inside a multilayer is described with a reasonable accuracy, but overall, it allows representing in a simple way a variety of deposition process and defect seeds.

In order to compute the parametric equation of the parallel curves in 3D for an axisymetric geometry, it is easier and faster to compute twice 2D parametric equations of the parallel curves[14]: Once following x direction and once following the y direction.

$$\begin{cases} x_p(t) = x(t) + d.\dfrac{z'(t)}{\sqrt{x'(t)^2 + z'(t)^2}} \\ z_p(t) = z(t) - \alpha.d.\dfrac{x'(t)}{\sqrt{x'(t)^2 + z'(t)^2}} \end{cases} \qquad \text{Eq. 11}$$

$$\begin{cases} y_p(t) = y(t) + d.\dfrac{z'(t)}{\sqrt{y'(t)^2 + z'(t)^2}} \\ z_p(t) = z(t) - \alpha.d.\dfrac{y'(t)}{\sqrt{y'(t)^2 + z'(t)^2}} \end{cases} \qquad \text{Eq. 12}$$

In order to take into account the possible planarizing (or widening) effect due to the characteristics of the deposition process, a parameter α is inserted in the parametric equations.

$\alpha < 1$ means that the height of the image of the defect on top of the mask is higher than the height of the defect seed.

$\alpha = 1$ represents a conformal deposition process; the height of the image of the defect on top is the same than those of the defect seed.

$\alpha > 1$ represents a planarizing effect; the height of the image of the defect on top is lower than those of the defect seed.

These three different configurations are shown in the three following figures (Figure 6 a,b & c):

Our standard deposition process (based on Ion Beam Sputtering) is very close to be conformal. A very slight planarization effect can be observed this mean that a paramater α very close but larger than 1 is a good approximation of this process.

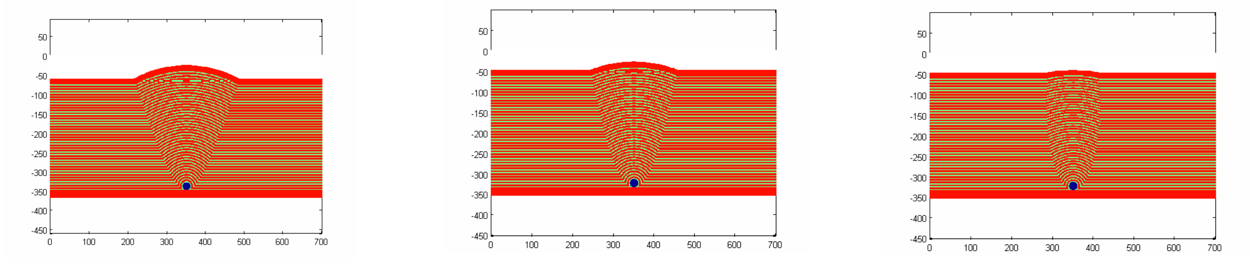

a) $\alpha < 1$: widening effect

b) $\alpha = 1$: Conformal effect

c) $\alpha > 1$: Planarizing effect

Figure 6 : Representation of three different conditions of deposition process.

3.2. Influence of the parameters on the aerial image and on the CD

3.2.1. Influence of the defect size for a conformal deposition model

In this section, we compare the influence of a defect on the aerial image for three different sizes of defect seed: 10nm, 50nm and 100nm diameter. The α value is 1. The MMFE allows computing the intensity of the near field above the EUV mask. This intensity is represented for the three different size of defect on Figure 7.

The light incidence is defined for these parameters: $\theta=5°$, $\phi=0°$, $\delta=180°$. On the figure of near field intensity, it corresponds to a light coming from the bottom of the figure as represented by the blue arrow.

The magnitude and the phase of the electric field allow determining the aerial image. The illumination conditions used are the following: NA = 0.3, $\sigma = 0.7$, $\lambda = 13.5$nm. 2D maps of the aerial images are shown in Figure 8:

A cross section along the y direction is more convenient to see clearly the drop of light intensity induced by the defect. It is represented Figure 9.

The cross sections show that the drops of intensity for the three different sizes are very important. The defect will print in the resist even for a low threshold whatever the size. The lowest level of intensity is the same for a defect seed with 50nm diameter and for a defect seed with 100nm diameter. The only main difference according to the different defect appears on the width of the intensity dip. Obviously, the figures show that the smallest defect seed will lead to the smallest CD.

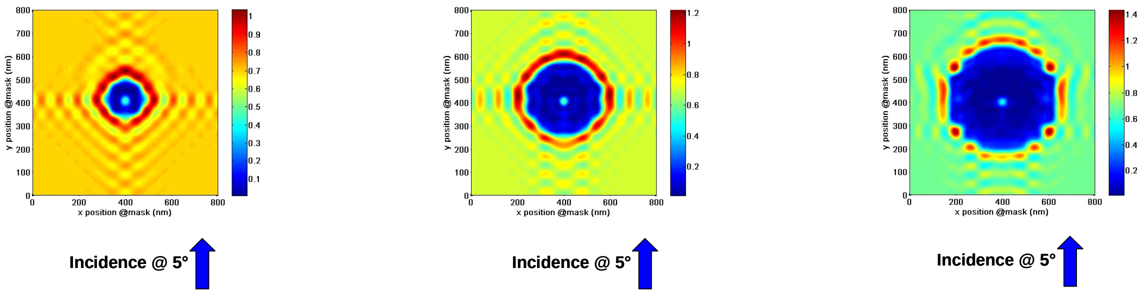

a) 10nm spherical seed b) 50nm spherical seed c) 100nm spherical seed

Figure 7 : Intensity of the near field above the mask for three different sizes of defect.

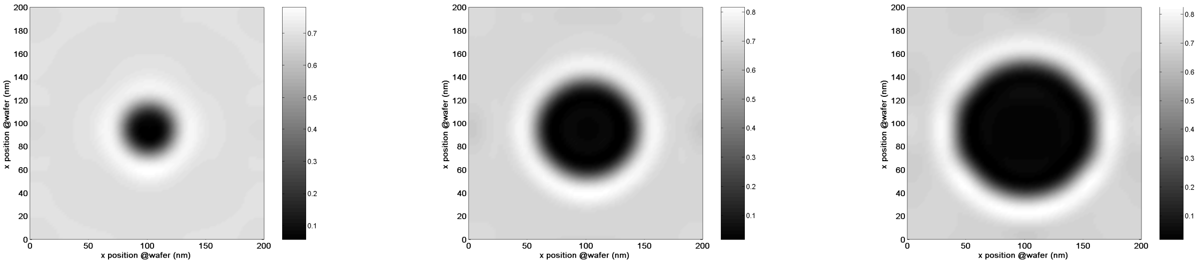

a) 10nm spherical seed b) 50nm spherical seed c) 100nm spherical seed

Figure 8 : Aerial image of three different sizes of defect for conformal deposition process

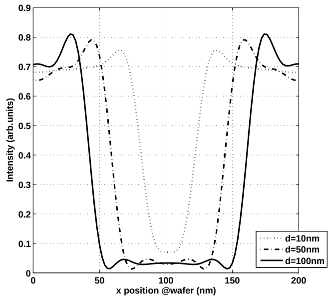

Figure 9 : Cross section of the aerial image of three different sizes of defect for conformal deposition process

3.2.2. Influence of the deposition process

In section 3.2 it has been shown that the conformal model of the deposition process leads to a printable defect even for the smaller seed size of 10nm. It is now interesting to see the influence of the deposition process on the printability. This study is performed for a small defect (of 10nm) which is not able to be printed. Three values of α parameter are considered: $\alpha = 0.96$ (widening or amplified effect), $\alpha = 1$ (conformal), $\alpha = 1.06$ (planarizing effect).

In the aerial image cross section (Figure 10) the drop of intensity is small for the planarizing situation. Whatever the threshold of printability of the resist, the defect will not print in the resist.

The planarizing deposition process aims at reducing the disturbance of a defect seed inside the multilayer on the reflected intensity of the electrical field. If the defect seed dimension is relatively small (lower than 10nm) it can be too weak to be printed on the resist as shown on Figure 11.

For large defects (larger than 10nm) the planarizing effect reduces the printed feature size compared to conformal and widening effects. But this improvement remains not sufficient to avoid the defect to print.

For small defects, the conformal and widening deposition processes leads to a printing of defects whereas the planarizing effect allows hiding the presence of a defect seed inside the multilayer.

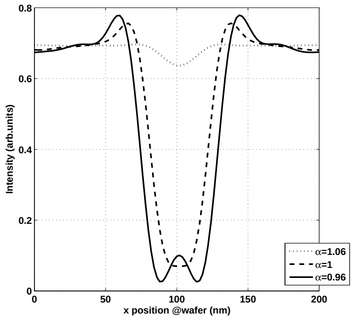

Figure 10 : Cross section of aerial image of three different deposition processes for a 10nm defect seed.

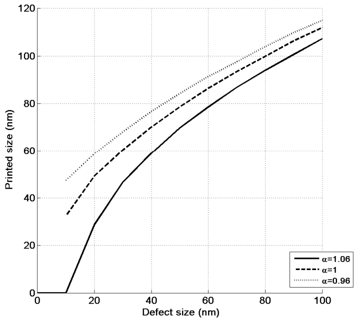

Figure 11 : Size of the printed feature versus size of defect (spherical) for a threshold at 0.25.

4. 3D DEFECT CLOSE TO AN ABSORBER PATTERN

In the section 3, the influence of a defect on the reflection of a Bragg mirror used in the EUV mask blank has been shown. Considering the EUV mask topography, the defect can be located more or less close to an absorber pattern. The goal of this study is to analyse the influence of a defect on the pattern print in the resist versus the size and the position of the defect.

Figure 12 shows an example of a cross section of a 3D EUV mask structure with a spherical defect seed sitting at the bottom of a multilayer and close to an absorber line for various horizontal positions.

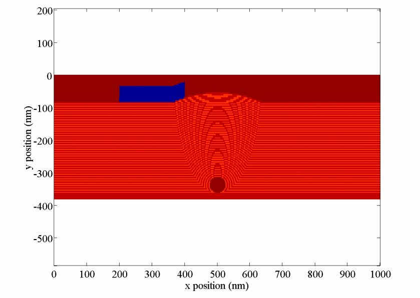

Figure 12 : Cross section of a 3D defective EUV mask structure.

4.1. Influence of the defect position.

The parameters of the 3D defective EUV mask are the following:

- Spherical defect shape with 10nm diameter seed.
- Conformal deposition (α = 1)
- Absorber line of 48nm in width (this is in agreement with the gate length of a MPU at the 22nm node given in the ITRS roadmap).
- The illumination conditions used are the following: NA = 0.3, σ = 0.7, λ = 13.5nm.

The obtained aerial images are represented in Figure 13. The distance mentioned corresponds to the distance on the mask between the middle of the absorber line and the middle of the defect.

The corresponding cross sections are shown in Figure 14. The drop of intensity in the middle of the picture is due to the defect and the moving dip is due to the absorber line.

These different configurations show that for a defect far from the absorber pattern, the effect of the absorber and the one of the defect are independent and lead to two different drops of intensity (Figure 14.a). Consequently, the printed CD of the absorber line has the same width than in the case of a non defective mask. With the distance reduction, the two dips come closer but with no influence on the printed CD (Figure 14.b & Figure 14.c) until the level of intensity between the two dips is lower than the threshold of printability in the resist (Figure 14.d). This configuration leads to the largest printed CD and thus, the worst position for a defect. When the defect and the absorber line are very close, the printed CD is reduced. Finally, when the defect is just underneath the absorber, the width of the global printed CD will depend of the size of the defect on top of multilayer stack. If the disturbance due to the defect is smaller than the absorber line, the influence of the defect on printed CD will be hidden by the absorber. But, if the width of the printed CD of the defect at the given threshold is larger than the absorber line, it will have an impact on the printed CD of the absorber line (Figure 13.f and Figure 14.f). This evolution of the printed CD is summarized with the Figure 15.

These results have been obtained for a threshold of 0.25, the absorber line width is 48nm at mask scale. The defect has a spherical shape generated by a 10nm diameter seed.

In Figure 15, the printed CD of the absorber line is defined for two deposition process parameters. For the conformal, the curve follows the explanations describes in the previous paragraph. For the planarizing process, for a small defect size (10nm), the defect is not printed therefore it has no influence on the printed CD. The resulting printed CD remains constant and corresponds to the printed CD of the absorber line alone.

Note that in the conformal model, with the behaviours described above (printed CD of the defect larger than the printed CD of the absorber line), the resulting printed CD is larger than the printed CD of the absorber line when the absorber is just on the defect. This would be different if the width of the absorber line were larger. Indeed for a large absorber which covers the whole defect perturbation on top of the multilayer, the final value, for the defect placed just underneath the absorber line, would reach the same value than the printed CD of the absorber line. On Figure 15, the blue and the red curves would cross at 0.

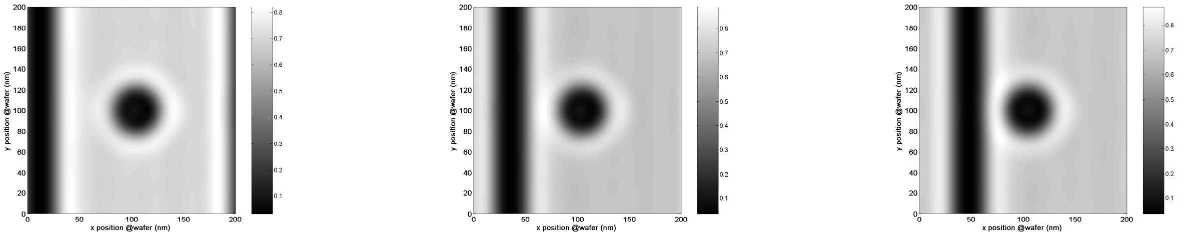

a) Distance (mask scale) : 376nm *b) Distance (mask scale) : 280nm* *c) Distance (mask scale) : 184nm*

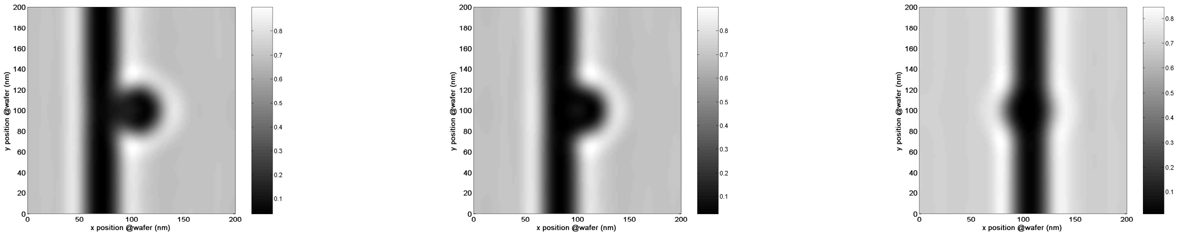

d) Distance (mask scale) : 136nm *e) Distance (mask scale) : 88nm* *f) Distance (mask scale) : -8nm*

Figure 13 : Aerial images for different absorber line position regarding the defect position.

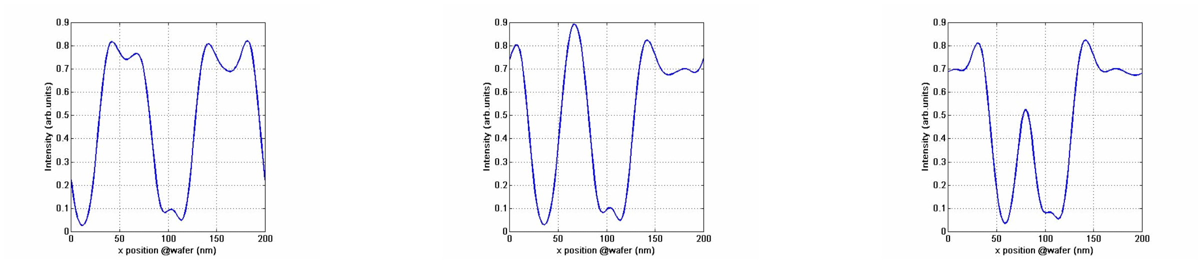

a) Distance (mask scale) : 376nm

b) Distance (mask scale) : 280nm

c) Distance (mask scale) : 184nm

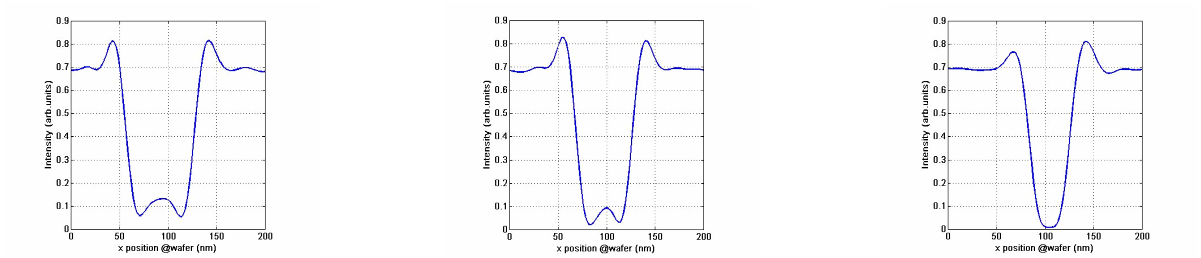

d) Distance (mask scale) : 136nm

e) Distance (mask scale) : 88nm

f) Distance (mask scale) : -8nm

Figure 14 : Cross section of aerial images for different absorber line position regarding the defect position

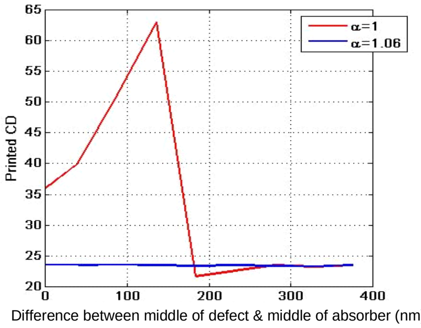

Figure 15 : Printed CD of the absorber line regarding the position of the defect.

5. CONCLUSION

The influence of a 3D defect inside a EUV mask structure has beenanalyzed by simulation. The method used to address this kind of topography is the MMFE, often used in 2D simulation because it is fast and well adapted for the EUV lithography simulation. The extension of this method in 3D has been presented. This modal method allows considering many different shape of defects. For sake of simplicity, only the spherical shape for the defect has been addressed. This paper underlines the importance of the deposition process to hide the effect of the defect within the multilayer stack. The three models of deposition process (conformal, planarizing and widening) show that for conformal and widening, even if the defect is small (lower than 10nm), it can be printed. This is not true anymore with the planarizing model. It is still hard to consider a model very close to an experimental deposition process; nevertheless, the conformal one seems to be the closer. Indeed, experimental measurements have shown that the height of the defect on top of multilayer do not undergo a large compression effect whereas the width becomes larger.

For a defect close to an absorber, the influence on the printed CD has been shown. Many parameters must be considered to address a realistic structure, namely the size of the absorber line, the shape of the defect, the position of the defect regarding the absorber line position, the deposition process and the threshold of printability in the resist. This last parameter will determine the position of the defect where the two dips of intensity due to the absorber pattern and to the defect will merge to create a single print.

Finally this simulation tool is able to model defective EUV masks with a behavior very close to the experimental process. Additional work will be done to improve the computing time in 3D and, arbitrary models of deposition process can be implemented that match the experimental results.

ACKNOWLEDGEMENT

Aerial image computations are performed using a software tool developed by the simulation group of the Fraunhofer Institut Erlangen (Dr A. Erdmann).

BIBLIOGRAPHY

---

[1] E. M. Gullikson, C. Cerjan, D. G. Stearns, P. B. Mirkarimi, and D. W. Sweeney: *J. Vac. Sci. Technol. B 20* (2002), 81.

[2] P. Evanschitzky, A. Erdmann, M. Besacier, and P. Schiavone: *Proc. SPIE Conf. Photomask and Next-Generation Lithography Mask Technology X*, 2003, vol. 5130, p. 1035.

[3] M. Besacier, P. Schiavone, V. Farys, R. Smaali, *Proc. SPIE conf. Microlithography*, 2005, vol. 5751, pp 629-639.

[4] P. B. Mirkarimi & Al, *JM3 3,139* (2004).

[5] V. Farys & Al, *Applied Physics Letters vol. 87*,1, (2005)

[6] E.Quesnel, J.Hue, V.Muffato**,** C.Pellé and P.Lamy, *J. of Vac. Sci. Technol. B 22*(5), Sep/Oct 2004

[7] V. Farys & Al, *J. Vac. Sci. Technol. B 23(6)*, pp 2860 – 2865, Nov/Dec 2005

[8] M.G Moharam, T.K. Gaylord, J. *Opt. Soc. Am., vol.72, pp 1385 – 1392* (1982)

[9] R. Bräuer and O. Bryngdahl, *Opt. Commun.. 100*, 1-5 (1993).

[10] S. Peng, G.M. Morris, *J. Opt. Soc. Am. A, vol.12, n°5*, pp 1087 – 1096 (1995)

[11] G. Granet, . *J. Opt. Soc. Am. A, vol.16, n°10*, pp 2510 – 2516 (1993)

[12] L. Li, *J. Opt. Soc. Am. A, Vol. 14, No 10*, pp 2758-2767 (1997).

[13] T.Pistor, Y. Deng, A. Neureuther, *J Vac. Sci. Technol., B 18(6)*, pp 2926, Nov/Dec (2000).

[14] X. Lee: http://www.xahlee.org/SpecialPlaneCurves_dir/Parallel_dir/parallel.html.